

Highly Luminescent Gold Nanocluster Frameworks

Sourov Chandra,* Nonappa, Grégory Beaune, Anirban Som, Shaochen Zhou, Jouko Lahtinen, Hua Jiang, Jaakko V. I. Timonen, Olli Ikkala, and Robin H. A. Ras*

Metal nanoclusters (NCs) are being intensely pursued as prospective luminophores because of their tunable electronic and optical properties. Among the various fluorescent NCs, gold nanoclusters (GNCs) are attractive due to their biocompatibility and excellent photostability, even if so far, they have had limited application potential due to poor quantum yield (QY). In this context, a facile route is demonstrated to tune up the photophysical and photochemical activities of water-borne luminescent GNCs through the formation of self-assembled nanocluster superstructures. The approach involves the controlled introduction of Sn²⁺ ions, directing GNCs from individual particles into 3D spherical gold nanocluster colloidal frameworks (GNCFs). In these, the reduction in the nonemissive relaxation pathways leads to significant enhancement of luminescence signals (QY from ≈3.5% to ≈25%), likely owing to restricted movements of ligands. This approach paves ways for GNCFs as a potent agent for biomedical imaging and therapies, while their high photocatalytic activity is an added advantage.

cytotoxic and are restricted in their use in nanomedicine.^[6] Organic dyes, on the other hand, suffer from toxicity and poor photostability.^[7] Therefore, the large potential of appropriate luminophores in biomedical applications has prompted intensive efforts toward the development of alternative nanomaterials with reduced toxicity and increased biocompatibility. A promising new approach is to exploit the photoluminescence of noble metal nanoclusters (NCs), having emissions in visible or near-IR regions, depending on their size, chemical environments, and surface ligands.^[8]

Few-atom metal NCs, with a core diameter of ≤1 nm, possess unique optical properties, stemming from quantum confinement of the electrons, unlike larger plasmonic nanoparticles.^[1,9] Among the metal nanoclusters, atomically precise gold

1. Introduction

Luminophores, the luminescent particles or compounds, have a remarkable impact due to their successful integration into optoelectronic devices, diagnostics, and sensors.^[1] Ultrabright luminophores with narrow emissions, large Stokes shift, and supreme photostability offer possibilities for specific visualization of intracellular processes at single particle level.^[2] However, it is still a great challenge to develop such water-borne biocompatible photoluminescent nanomaterials, especially for biomedical applications.^[3–5] Semiconductor nanocrystals, while revered as versatile and potent luminescent probes, generally contain heavy metal atoms. Therefore, most of them are highly

nanoclusters (GNCs) have gained remarkable interest over the last decade due to their high stability and biocompatibility.^[9,10] However, low photoluminescence (PL) quantum efficiency restricts their potential applications.^[11,12] PL can be amplified to a certain extent by the reduced rotational degree of freedom of the ligands surrounding the metal core, restrictions of intramolecular motions, or preventing nonradiative relaxations through aggregation.^[13–16] However, controlling the aggregation behavior of the NCs to obtain superstructures of defined morphology in aqueous media has been a challenge.^[17] Therefore, it is relevant to ask whether controlled self-assemblies can be designed to achieve colloidal superstructures based on luminescent NCs with enhanced PL and quantum yields in aqueous dispersion. Despite their dispersion behavior being similar to supramolecular complexes, self-assembly of monolayer protected NCs is a challenging task, as the inter-nanocluster interactions are close to the thermal fluctuations of the surroundings. Recently, it has been shown that atomically precise gold nanoclusters with surface carboxylic acid functionalities offer control over self-assemblies in aqueous medium to 2D or 3D superstructures.^[18–20]

We have discovered that a controlled assembly of water soluble luminescent GNCs having surface carboxylic groups by introducing metal ions might offer a new avenue to achieve superstructures, consisting of GNCs, metal ions, and ligands, akin to metal–organic frameworks. Such cluster frameworks would allow restricted motion of the surface ligands, thus potentially enhancing the PL. To test this hypothesis, we used water-soluble glutathione (GSH) capped luminescent

Dr. S. Chandra, Dr. Nonappa, Dr. G. Beaune, Dr. A. Som, S. Zhou, Dr. J. Lahtinen, Dr. H. Jiang, Prof. J. V. I. Timonen, Prof. O. Ikkala, Prof. R. H. A. Ras

Department of Applied Physics
School of Science
Aalto University

02150 Espoo, Finland


E-mail: sourov.chandra@aalto.fi; robin.ras@aalto.fi

Dr. Nonappa, Prof. O. Ikkala, Prof. R. H. A. Ras

Department of Bioproducts and Biosystems
School of Chemical Engineering

Aalto University

02150 Espoo, Finland

 The ORCID identification number(s) for the author(s) of this article can be found under <https://doi.org/10.1002/adom.201900620>.

DOI: 10.1002/adom.201900620

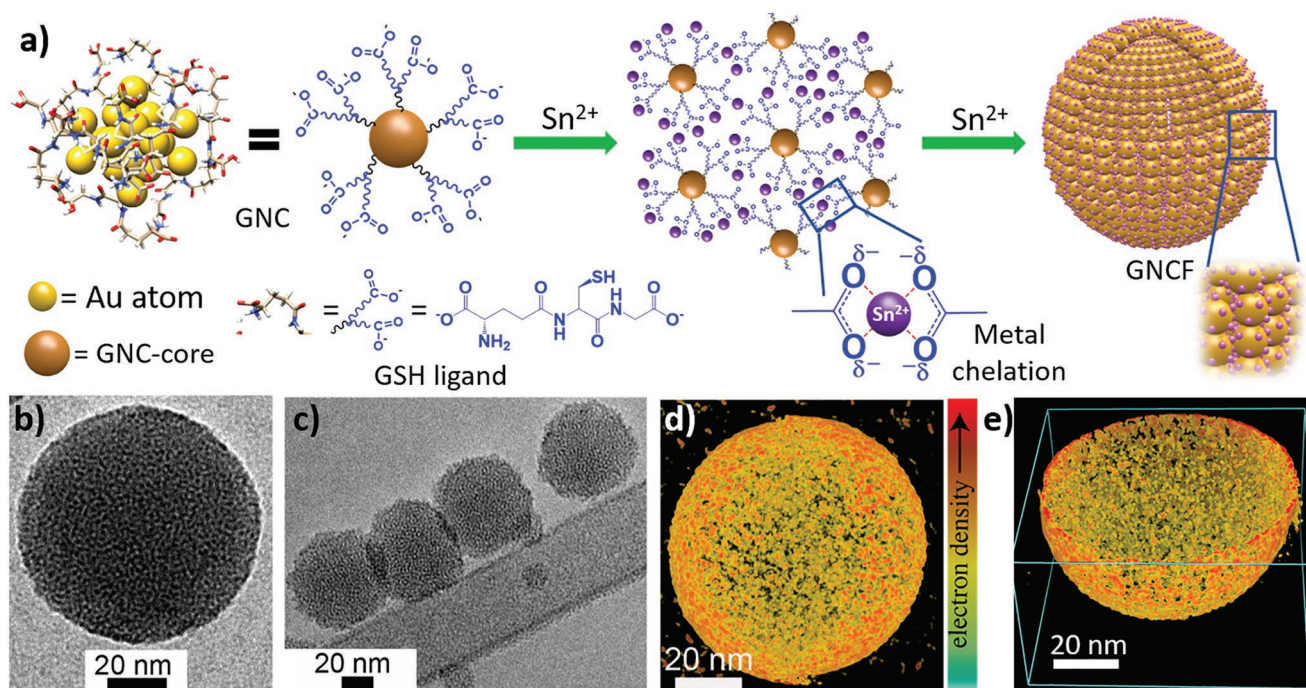


Figure 1. a) Representation of a luminescent GSH-encapsulated GNC, the possible interactions in between the metal ions and COO^- groups of the ligand over GNCs through chelation, and the schematic illustration for the formation of GNCFs. b) HR-TEM micrograph of GNCF-100 dispersed in water, c) cryo-TEM micrograph of GNCF-100, d) electron tomography (ET) reconstruction of a GNCF-100, and e) its cross-sectional view.

GNCs. The controlled assembly of GSH–GNCs was achieved by introducing Sn^{2+} ions, which directs the inter-nanocluster cross-linking through the negatively charged surface carboxylate ($-\text{COO}^-$) groups. Using cryogenic transmission electron microscopy (Cryo-TEM) and electron tomography (ET), we have shown that the resulting structures are spherical framework materials with tunable sizes. Our results reveal that the gold nanocluster framework (GNCf) assemblies show an unprecedented seven-fold increment in the quantum yield compared to that of individual GNCs, when Sn^{2+} is used as a cationic cross-linker. We further demonstrate that the self-assembled GNCfs with extremely high PL in aqueous medium are nontoxic, and possess excellent photocatalytic activity compared to the traditional plasmonic gold nanoparticles, and, more importantly, far better than that of GNC itself. Therefore, it is expected that the GNCfs, by means of their unique architecture and biocompatibility, would pave way for water dispersible colloidal framework materials for biomedicine and catalysis.

2. Results and Discussion

2.1. Synthesis, Morphology, and 3D Reconstruction of Gold Nanocluster Frameworks

GSH encapsulated gold nanoclusters are synthesized and characterized according to the reported procedure.^[13] High-resolution transmission electron microscopy (HR-TEM) images confirm the formation of very small particles of GNCs with an average size of 1 nm (Figure S1, Supporting Information). To achieve higher-order structures, various metal ions

(Cs^+ , Mn^{2+} , Pb^{2+} , Cd^{2+} , Sn^{2+} , Zn^{2+} , Fe^{3+} , Al^{3+} , and Sn^{4+}) in the form of their chloride salts are introduced into the aqueous dispersion of GNCs. Among all the tested metal ions, only the addition of Sn^{2+} dramatically changes the luminescent properties. Metal chelation induced assembly of GNCs into GNCfs is schematically represented in **Figure 1a**. HR-TEM (Figure 1b) and Cryo-TEM (Figure 1c) imaging of the aqueous dispersions reveals the formation of higher-order spherical superstructures. Resolving the 3D structures using ET reconstruction confirms the spherical nature of colloidal superstructure, where GNCs are uniformly filled up, due to assembly of nanoclusters (Figure 1d,e; Videos S1 and S2, Supporting Information). Since the cluster assemblies are directed by the interaction between divalent metal ions and the carboxylic acid groups of GSH on nanoclusters, we denote the superstructures as gold nanocluster frameworks. To monitor the effect of Sn^{2+} concentration on the structure and stability, a systematic study was performed by adding varying amounts (10–400 μL) of $10 \times 10^{-3} \text{ M}$ aqueous solution of SnCl_2 , while keeping the GNC concentration constant (400 μL , 1.875 mg mL^{-1}). The resulting superstructures are designated as GNCf-10, GNCf-20, GNCf-40, GNCf-60, GNCf-80, GNCf-100, GNCf-200, GNCf-300, and GNCf-400 by introducing 10, 20, 40, 80, 100, 200, 300, and 400 μL of SnCl_2 , respectively. Subtilly exists as unstable dispersions have been obtained when the amount of Sn^{2+} is below 60 μL or above 500 μL . The GNCfs are distinct and well separated when the concentrations are in the range of 60–100 μL . However, higher concentration also leads to higher-order structures, as shown by scanning transmission electron microscopy (STEM) (**Figure 2**). The stability of the GNCfs also depends on the amount of Sn^{2+} , as zeta potential (ζ) is +12.4 mV for GNCs

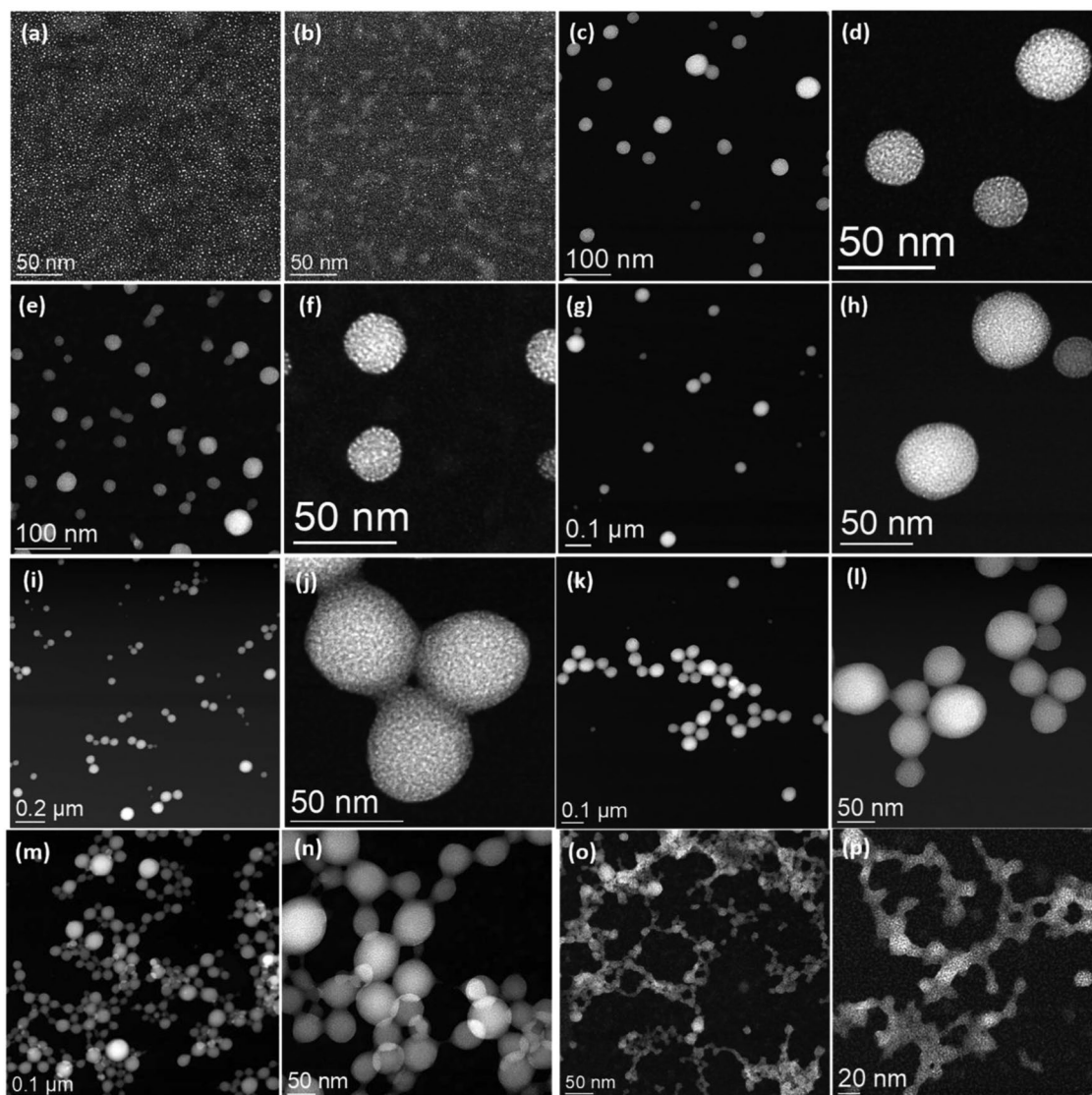


Figure 2. STEM micrographs of a) GNCs; b) GNCF-10; c,d) GNCF-40; e,f) GNCF-60 g,h) GNCF-100, i,j) GNCF-120, k,l) GNCF-200, m,n) GNCF-300, and o,p) GNCF-400.

at pH 7, increasing steadily upon higher concentration of Sn^{2+} and reaching the maximum for GNCF-300 with $\xi = +54.9$ mV (Figure S2, Supporting Information), combined with excellent colloidal stability. Aggregation was observed by adding lower concentration of Sn^{2+} ($<60 \mu\text{L}$) into the GNCs as further supported by dynamic light scattering studies. When $10 \mu\text{L}$ Sn^{2+} (GNCF-10) was added to a known amount of GNC dispersion, an immediate increase in the particle size from 3 to 191 nm was noticed. A stable dispersion was obtained in GNCF-80 with their average hydrodynamic diameter of 52 nm. Above this concentration, a linear increase in the size of the superstructures with increasing the concentration of Sn^{2+} was observed.

2.2. Surface Characterizations and Elemental Analysis

Deeper analysis using high-resolution STEM imaging^[21] supports that the aqueous superstructures are composed of GNCs

with chemical cross-links between their negatively charged ligands mediated by Sn^{2+} ions (Figure 3a). The degree of cross-linking upsurges with an increasing amount of Sn^{2+} , undergoing inter-nanocluster assembly to interframework cross-linking, ultimately leading to GNCF assemblies (Figure 2).^[22] The elemental compositions of GNCFs have been analyzed using energy-dispersive X-ray (EDX) mapping (Figure 3b; Figure S3, Supporting Information), additionally supported by X-ray photoelectron spectroscopy (XPS) (Figure S4, Supporting Information). EDX mapping reveals that both Au and Sn species are located within and over the GNCFs, and further confirms the presence of Au, Sn, C, N, S, and O elements in GNCFs by XPS analysis. Changes in the chemical environment upon addition of Sn^{2+} have been studied by analyzing high-resolution C1s photoelectron spectra (Figure 3c,d; Figures S5 and S6, Supporting Information). The deconvoluted peaks for both GNCs and GNCFs are observed at binding energies (BE) of

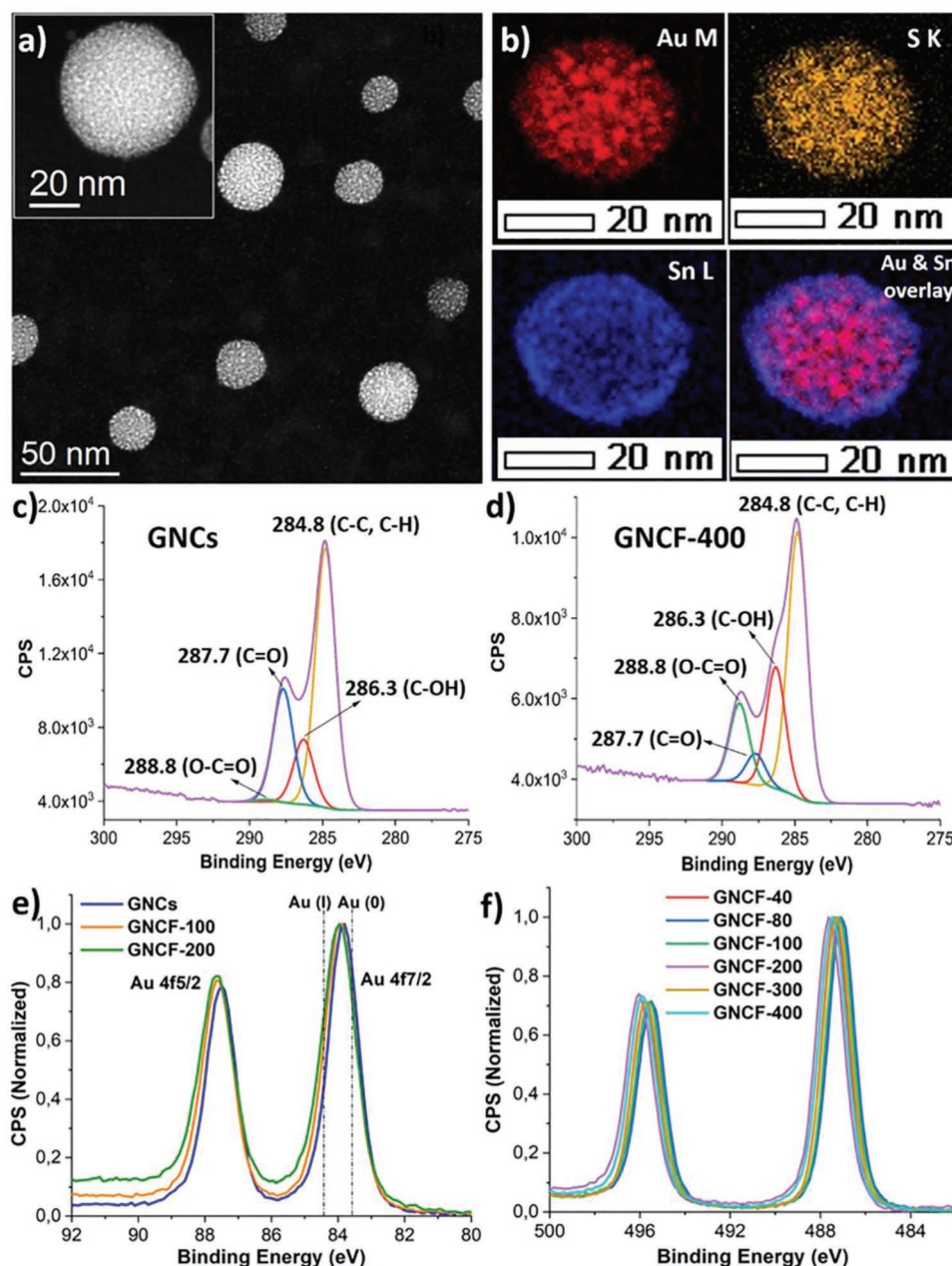


Figure 3. a) Dark field scanning transmission electron microscopy (DF-STEM) images and b) EDX mapping of GNCF-100. c) 1s XPS spectrum of c) GNCs and d) GNCF-400. e) Au 4f and f) Sn 3d XPS spectra of GNCs and GNCFs.

284.8, 286.3, 287.7, and 288.8 eV, which are attributed to C–C, C–H, C–O, C=O, and O–C=O bonds^[23] of GSH, respectively. Notably, significant changes in the relative intensities of the BE have been observed upon addition of Sn²⁺ to GNCs. In detail, the peak corresponding to C=O (287.7 eV) shows a decrease in the intensity, whereas the intensities of both C–O (286.3 eV) and O–C=O (288.8 eV) bands increase (Table S1, Supporting Information). So, it is concluded that there are strong electrostatic and coordination interactions between the metal ions and the carboxylic acid groups of the ligands, which diminish the double bond character of the C=O groups of GSH upon superstructure formation. Comparison between the Au 4f

photoelectron spectra (Figure 3e), Au 4f7/2 peaks appear at 83.8 and 83.9 eV for GNCs and GNCFs respectively. The results confirm the existence of a precisely similar chemical environment of gold atoms both in GNCs and GNCFs, containing Au (0) and Au (I) species.^[24] The nanocluster is, therefore, constructed by a metal core assembled with Au (0) atoms, surrounded by Au (I)-GSH species around its surfaces. The high-resolution Sn 3d photoelectron spectra of GNCFs (Figure 3f) display the peaks at 487.3 ± 0.3 and 495.7 ± 0.2 eV corresponding to Sn 3d5/2 and Sn 3d3/2 respectively, indicating the presence of Sn⁴⁺,^[25] possibly due to oxidation during sample preparation (drying) for XPS.

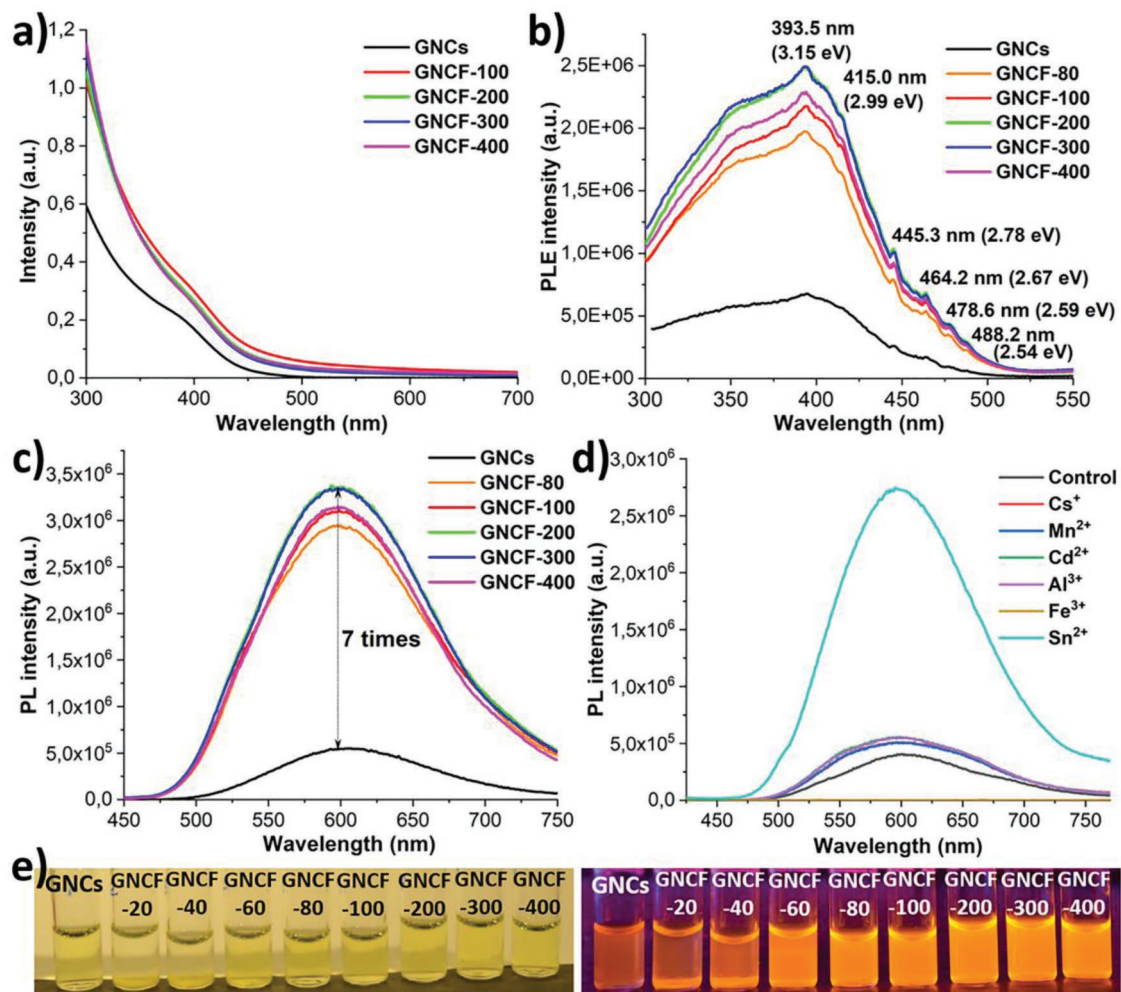


Figure 4. a) UV–visible absorption spectra, b) PLE spectra, and c) PL emission spectra of the GNCs and GNCFs. d) Comparison between the PL spectra of GNCs by introduction of different metal ions in water. e) Photographic images of the aqueous dispersions of GNCs and all GNCFs under visible light (left) and under UV irradiation (right).

2.3. Optical Properties, Correlation of PL Intensity, and Mechanisms

The UV–visible absorbance spectra for all the GNCFs in aqueous dispersion (Figure 4a) are found to be similar to that of the GNC itself with a characteristic peak at 395 nm.^[13,14] This suggests that the intrinsic properties of individual GNCs are retained, further supporting that the framework formation is predominantly through supramolecular interactions between the surface ligands and metal ions. Photoluminescence excitation (PLE) spectra (Figure 4b) of GNCFs at 590 nm emission wavelength reveal that the peak positions remain unaltered to that of GNCs, however leading to increased intensities. Importantly, unlike quantum dot based luminophores, GNCs or GNCFs presented in this work show multiple excitation peaks between 393.5 (3.15 eV) and 488.2 nm (2.59 eV). This indicates the existence of several intra-atomic and interatomic electronic transitions among ligand (GSH) to Au (0) core and concurrent Au (0) core to Au (I) surfaces.^[26] The PL emissions (Figure 4c) for GNCFs are significantly higher than that of the GNCs in

water. With increasing the concentration of Sn^{2+} , the PL intensity gradually increases with maximum intensity for GNCF-300. The absolute PL quantum yield for GNCF-300 is $\approx 25\%$, i.e., approximately sevenfold higher than that of the isolated GNCs. GNCFs emit bright yellowish-orange light in contrast to the weak emissions coming from the GNCs (Figure 4e). No superstructures were observed by using metal ions other than Sn^{2+} studied in this work, including monovalent, divalent, trivalent, and tetravalent ions (Figure S7, Supporting Information). Slight increments of PL emissions were recorded for Mn^{2+} , Cd^{2+} , and Al^{3+} due to random aggregation (Figure 4d).^[12,13] It is important to note that aggregation induced emissions of GNCs have shown two to three-fold increase of PL.^[14,27] By contrast, our results showing such a high increment of PL in solution by the addition of Sn^{2+} is attributed to the restricted motion of the ligands through orientation in framework structure and formation of continuous networks within the GNCFs.^[26,28] The formation of the well-defined superstructure of GNCs by introduction of Sn^{2+} ions, but not by other metal cations, might be due to the selective complexation of GSH

ligands over the nanocluster surfaces under the experimental conditions.^[29,30] Further, different metal ions also undergo solvation, where the geometry might greatly affect the complexation when dispersed in water as studied extensively by Cox et al.^[31]

It has been proposed that Au (I)-thiolate shell in the vicinity of Au (0) core contributes toward the intense luminescence through ligand-to-metal-to-metal charge transfer (LMMCT) mechanism.^[32] Therein, the metal–metal charge transfer originates from singlet state Au (0) core to triplet state (T1 or T2) of Au (I) shell, followed by the relaxation in the form of PL from T1 or T2 state of Au (I) shell to the highest occupied molecular orbital (HOMO) of Au (0) core. The well-defined nanocluster network through metal–ligand (Sn²⁺–GSH) interactions in these superstructural 3D architectures prohibits several nonradiative relaxation modes in GNCFs therefore, the strong luminescence primarily arises from the highly luminescent T1 state to Au (0) HOMO with an enhanced LMMCT relaxation mechanism.^[13,32] A slight PL blue shift may be due to the longer Au (I)–Au (I) distance in the nanocluster framework.^[27] The corresponding bandgaps (Figure S8, Supporting Information) were calculated according to the Tauc, Devis, and Mott equation^[33]

$$\alpha h\nu = K(h\nu - E_g)^n \quad (1)$$

where α is the absorption coefficient, $h\nu$ is the energy of the incident light, E_g is the optical energy gap or the bandgap, and n is a number which characterizes the optical absorption processes. For direct transition $n = 1/2$ and for indirect transition $n = 2$. For the high absorbing region, where α obeys the above

equation, by plotting $(\alpha h\nu)^2$ as a function of photon energy ($h\nu$) and extrapolating the linear regions of this curve to $(\alpha h\nu)^2 = 0$. The results demonstrating that the bandgap is almost unaltered before and after the formation of GNCFs from GNCs.

2.4. In Vitro Cytotoxicity and Bioimaging

Because of their excellent colloidal stability and high photoluminescence in aqueous medium, it is relevant to investigate whether GNCFs can be used for bioimaging purposes. To address this issue, we studied the cytotoxicity of GNCs and GNCFs by performing cell counting kit 8 (CCK-8) assay and trypan blue tests for two different cell lines (NIH3T3 and A549 cells).^[34] After incubation of cells with both GNCs and GNCFs, for 24 h and up to a concentration of 100×10^{-6} M, no obvious cytotoxicity was observed under the experimental conditions (Figure 5). More importantly, even in some cases, GNCFs exhibit higher viability compared to that of GNCs, especially at high concentration of the particles. Previously, similar observations have been reported in the literature on the effect of particle size on cell viability.^[35,36] A possible explanation could be the generation of reactive oxygen species by small nanoparticles.^[37] Moreover, small nanoclusters (GNCs) might aggregate in the cellular medium before their uptake, contrary to the larger ones (GNCFs), and cell death may occur because of the harmful effect of aggregates.^[36,38] To ensure the cell permeability and imageability of the GNCFs, both NIH3T3 and A549 cells are treated with an aqueous suspension of GNCF-200 and incubated for 24 h. Figure 6 and Figure S9 (Supporting

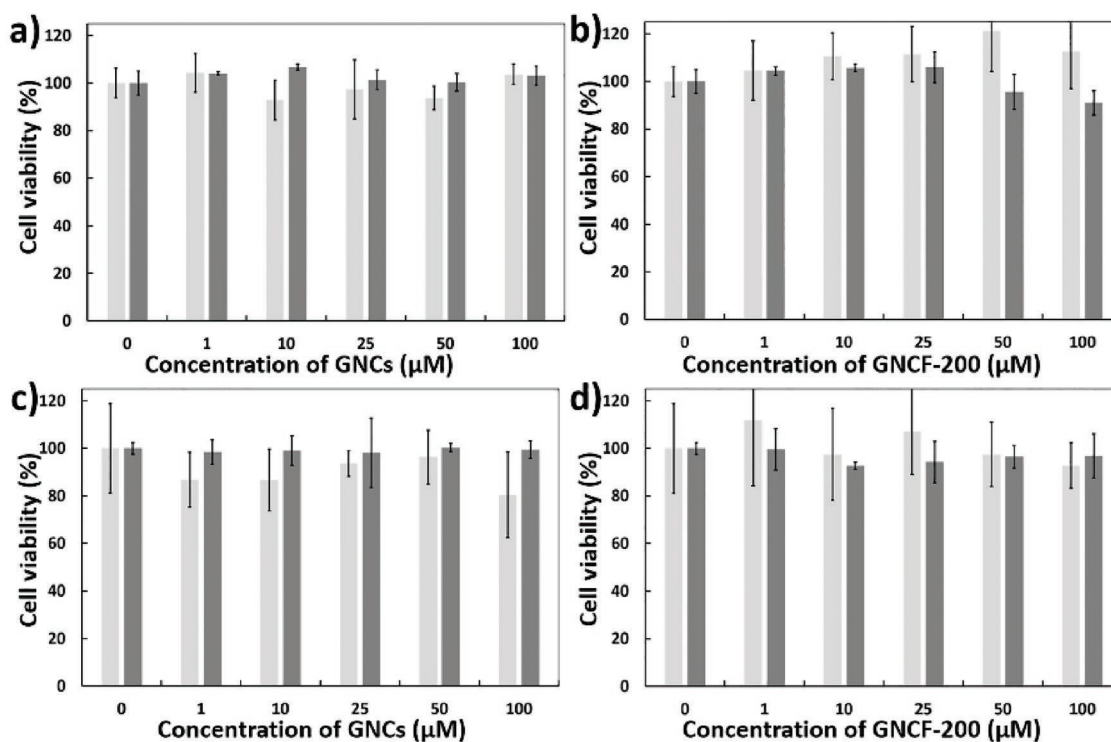


Figure 5. Cell viability using CCK-8 assay (light grey, $n = 3$) and the trypan blue test (dark grey, $n = 3$): on NIH3T3 cells, incubated with a) GNCs and b) GNCF-200; on A549 cells, incubated with c) GNCs and d) GNCF-200 for 24 h.

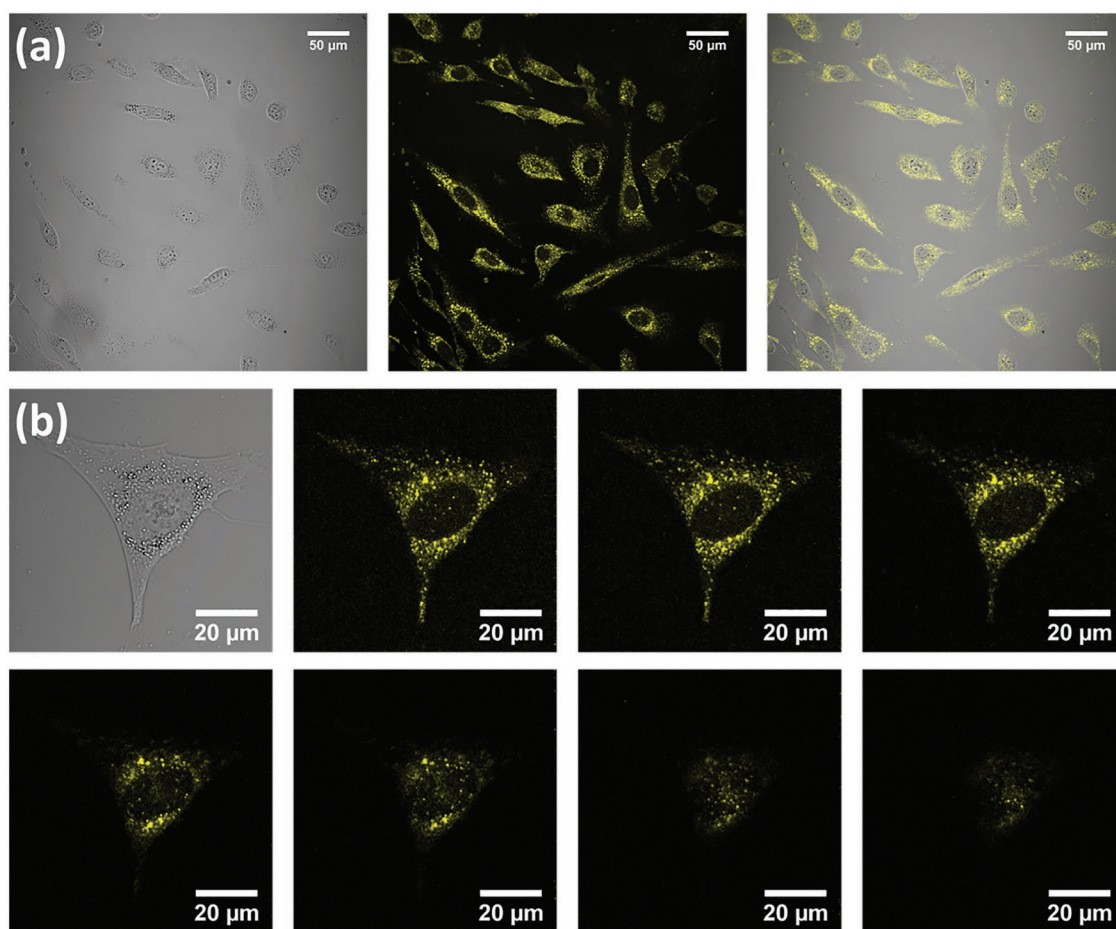


Figure 6. Confocal microscopy of NIH3T3 cells incubated with GNCF-200 (10×10^{-6} M) for 1 day in serum containing media (DMEM + 10% FBS). a) Bright field image (left), confocal fluorescence image (middle) and overlapped image (right) of a cell representative of the experiment. b) Bright field picture (top left) followed by images of a Z-stack (1.0 μ m intervals) of the same cell.

Information) reveal that the particles are located in the cells cytoplasm and emit brilliant fluorescent light at 458 nm excitation. Further analysis indicates that cells incubated with GNCF-200 are more permeable or brighter than that of the GNCs and thus easier to image cells (Table S2, Supporting Information).^[39]

2.5. Photocatalysis

Finally, we demonstrate that GNCFs can undertake high photocatalytic activity, allowing preliminary test on methylene blue (MB) degradation under both UV and visible light.^[40] Our results show that in the presence of GNCF-300 under UV irradiation (350 nm wavelength), complete degradation of MB occurs within 5.5 min (Figure 7a). By contrast, under similar conditions GNCs require 112 min. By contrast, in a control experiment, the degradation occurs without any catalyst by more than 140 min. The rate of degradation follows in the order of GNCF-300 > GNCF-200 > GNCF-100 > GNCs. The 20-fold to 25-fold increase in the photocatalytic activities of GNCFs is attributed to their 3D architecture with enhanced adsorption of the dye molecules over their surfaces and interiors, which would facilitate the exclusive catalytic activities of GNCFs with respect to

individual GNCs in water.^[41,42] Also, GNCFs exhibit high efficacy toward visible-light driven photoactivity compared to the GNCs itself. Figure 7b represents the concentration of MB with respect to the reaction time in the presence and absence of GNCs and GNCFs under blue light irradiation (455 nm wavelength). The photoactivity arises from the absorption of blue light and high catalytic network and surfaces, taking only 30 min to degrade the dye completely by using GNCF-300 as a catalyst. By contrast, GNCs have taken several days to complete the degradation procedure, whereas without catalyst the complete degradation of MB does not take place within a few days of our observation. While, in the absence of light (Figure S10, Supporting Information) or with the subsequent addition of Sn^{2+} ions into the reaction mixture in the absence of GNCs/GNCFs under UV-light, they exhibit a negligible or little effect on their catalytic activities (Figure S11, Supporting Information).

3. Conclusion

In summary, we have described a 3D superstructure of gold nanocluster frameworks with unprecedented augmentation of

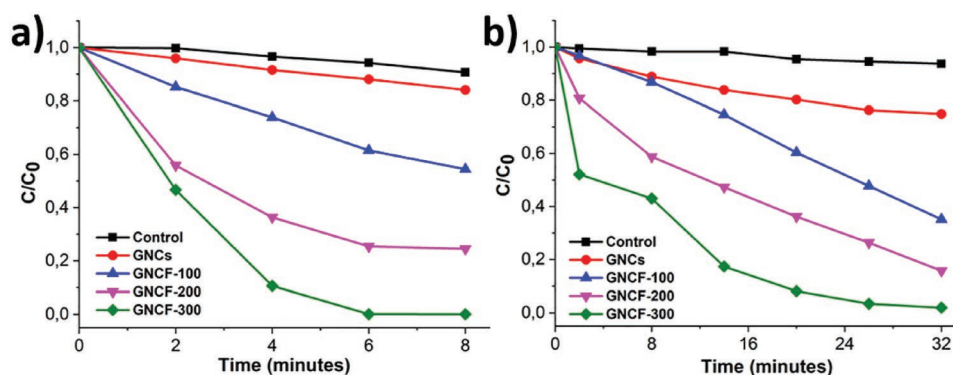


Figure 7. The rate of degradations of MB in presence of GNCs, GNCFs, and absence of a catalyst, excited at a) 350 nm and b) 455 nm wavelengths.

optical and catalytic properties. We studied the effects of different metal ions and their compositions on the structural and photo-physical properties of GNCs or GNCFs. Surprisingly, among all of the metal ions, only Sn^{2+} ions enabled the formation of super-structural frameworks from GNCs in solution phase by inter-cluster cross-linking through negatively charged GSH ligands over GNCs. This study leads the way toward water-borne medical imaging agents of low toxicity with strong emission, while their high photocatalytic activity is an added advantage.

4. Experimental Section

Materials: HAuCl_4 , SnCl_2 , glutathione (GSH), SnCl_4 , AlCl_3 , CsCl , FeCl_3 , CdCl_2 , ZnCl_2 , methylene blue, and H_2O_2 were received from Sigma-Aldrich.

Noncancerous murine fibroblasts cells (NIH3T3) and human epithelial carcinoma cells (A549) were used throughout the study. They were a generous gift from Dr. Apeksha Damania (Group of Prof. Kostianen, Department of Bioproducts and Biosystems, Aalto University—School of Science, Finland).

Synthesis of Gold Nanoclusters: Gold nanoclusters were synthesized according to Luo et al.^[13] Briefly, 20×10^{-3} M 500 μL of $\text{HAuCl}_4 \cdot 3\text{H}_2\text{O}$ was mixed into 4.35 mL of Milli Q (18 Ω) water at 25 °C with gentle stirring over a magnetic stirrer. After that, 150 μL (100×10^{-3} M) aqueous solution of glutathione was introduced into the above reaction mixture. The stirring was continued for another 10 min until a colorless solution was obtained. The mixture was heated at 70 °C for 24 h in an oil bath. Finally, the solution was cooled at room temperature and stored at 4 °C inside a refrigerator.

Fabrication of Gold Nanocluster Frameworks: To 400 μL (1.875 mg mL^{-1}) aqueous dispersion of GNCs, a known amount of SnCl_2 solution (10×10^{-3} M) was added dropwise with constant stirring at 500 rpm for 10 min. 10, 20, 40, 60, 80, 100, 200, 300, and 400 μL aqueous solutions of SnCl_2 were used, and the resulting superstructures were denoted as GNCF-10, GNCF-20, GNCF-40, GNCF-60, GNCF-80, GNCF-100, GNCF-200, GNCF-300, and GNCF-400, respectively. The final volume was adjusted at 800 μL for each set of reaction. The addition of metal salts induced the spontaneous superstructure formation, and the GNCFs were produced within 10 min. Finally, GNCFs were stored at 4 °C inside a refrigerator.

Microscopy and Spectroscopic Characterizations: HR-TEM and STEM were performed using JEM-2800 high-throughput analytical HR-TEM (JEOL) and JEM-2200FS Double Cs-corrected transmission electron microscope, respectively. Both instruments were operated at an acceleration voltage of 200 kV with field-emission guns. Specimen for HR-TEM and STEM analyses were prepared by drop-casting from the aqueous dispersions of the samples in ultrathin-carbon (<10 nm thickness) coated copper grids. The cryo-TEM images were collected

using JEM-3200FSC field-emission microscope (JEOL Ltd.) operated at 300 kV in bright-field mode with Omega-type zero-loss energy filter. Prior to sample preparation, 200 mesh copper grids with lacey carbon support film (Electron Microscopy Sciences) were plasma cleaned using Gatan Solarus (Model 950) plasma cleaner for 30 s. The samples for Cryo-TEM imaging were prepared by placing 3 μL of a freshly prepared aqueous dispersion of the sample on a plasma treated TEM grid and plunge-freeze into -170 °C ethane/propane mixture using Vitrobot 2 s blotting time under 100% humidity. The vitrified specimens were cryo-transferred to the microscope. The images were acquired with Gatan Digital Micrograph software, while the specimen temperature was maintained at -187 °C. UV-visible absorption spectra were recorded on a UV-Vis-NIR Agilent Cary 5000 spectrophotometer. PL and PLE spectra were obtained with a QuantaMaster 40 fluorescence spectrometer. The absolute PL quantum yields were measured by using a C9920-03G system equipped with a 150 W xenon lamp (Hamamatsu Photonics Co. Ltd., Japan). Zeta potential measurements were performed using Malvern Zetasizer Nano-ZS90. XPS was performed in Kratos Axis Ultra ESCA X-ray photoemission spectrometer using $\text{AlK}\alpha$ ($E = 1486.6$ eV) radiation. The X-ray source was operated at 15 mA and 15 kV and the analyser pass energy was 20 eV for high resolution scans and 80 eV for the survey spectra. The pressure in the analysis chamber was about 8×10^{-8} Pa during the measurements. The BE scale was referenced to 284.8 eV as determined by the location of the maximum peak on the C1s spectra, associated with adventitious carbon. The accuracy of the BE determined with respect to this standard value was within ± 0.1 eV.

Serial EM and Electron Tomography Reconstruction: The 3D reconstruction of the spherical cluster frameworks was achieved using by collected tilt series according to previously reported sample preparation procedures.^[17,43] In short, tilt series were acquired with the Serial EM-software package.^[44] Specimen was tilted between $\pm 69^\circ$ angles with 2° – 3° increment steps to collect stack files. The original stack files were then subjected for fine alignment and cropping with an open source set of image processing, modeling and display (IMOD) programs.^[45] The images were binned twice to reduce noise and computation time. Maximum entropy method^[46] reconstruction scheme was carried out with a custom-made program on Mac or Linux cluster with a regularization parameter value of $\lambda = 1.0e^{-3}$. Volumetric graphics and image analyses were performed with the UCSF Chimera package.

Cytotoxicity Studies: Trypan blue test: The cells were seeded in a 24-wells plate (BioLite Cell Culture Treated Plates, Thermo Scientific Co.) containing Dulbecco's modified Eagle's medium (DMEM) supplemented with 10% fetal bovine serum (FBS) and antibiotics (100 $\mu\text{g mL}^{-1}$ streptomycin and 100 U mL^{-1} penicillin) at 37 °C under a 95% air/5% CO_2 atmosphere (ICO50 CO_2 incubator, Memmert Co.). After 1 day, the cell culture medium was removed in each well and a fresh medium is added with increasing concentrations of gold clusters (GNCs or GNCF-200; 0, 1, 10, 25, 50, and 100×10^{-6} M; from 0 to 50 μL). The total volume of medium and gold clusters in each well was 500 μL and the cells were further incubated for 1 day. The cells were washed once with phosphate buffered saline (PBS) and trypsinized (200 μL per

well, 10 min in the incubator). Trypan blue (0.4% wt/vol, 12.5 μL) was added to an aliquot of the cell suspension (50 μL) and incubated for 5 or 10 min at room temperature. The viable cells (≈ 100 cells per sample) were counted by bright field microscopy. The viability values of the cells treated with gold clusters are expressed as a percentage of the viability of control cells. All experiments have been repeated three times.

CCK-8 Assay: The cell viability was checked using a CCK-8 kit (Sigma Aldrich Co.) according to the manufacturer's instructions. Briefly, a cell suspension (100 μL , 5×10^3 cells per well) was dispersed in a 96-well plate containing DMEM medium supplemented with 10% FBS and antibiotics (100 $\mu\text{g mL}^{-1}$ streptomycin and 100 U mL^{-1} penicillin). The plate was preincubated at 37 $^\circ\text{C}$ under a 95% air/5% CO_2 atmosphere for 1 day. Then, gold clusters suspensions (GNCs or GNCF-200, 10 μL) were added into the wells to final concentrations of 0, 1, 10, 25, 50, and 100 $\times 10^{-6}$ M. The plate was incubated for 1 day under the same conditions mentioned above. A CCK-8 solution (10 μL) was added to each well and the plate was incubated for 2 or 4 h in the incubator. Finally, the absorbance at 450 and 650 nm of each well was measured using a Synergy H1 hybrid microplate reader (BioTek). All experiments have been repeated three times.

Cellular Uptake and Confocal Microscopy: Cells were plated on glass cover slips at a concentration of 2×10^4 cells per mL. They were treated with the particle suspension (GNCs or GNCF-200, 10×10^{-6} M) and incubated for 24 h. They were washed with PBS buffer, dispersed in PBS, and directly observed. Cells were imaged and recorded by confocal microscopy (LSM 710, 20 \times /1.0 water immersion objective, $\lambda_{\text{ex}} = 458$ nm, $\lambda_{\text{em}} = 465\text{--}710$ nm). Images were exported from the instrument software (Zeiss Zen Black) in CZI format and further processed with Fiji (version 1.52d). In order to compare the cell permeability and imageability between GNCs and GNCFs, the average fluorescence of the cytoplasm (i.e., cell minus nucleus) of 15 NIH3T3 cells was determined incubated with GNCs and 15 other NIH3T3 cells incubated with GNCF-200 using ImageJ.

Photocatalysis and Dye Degradation: Photocatalytic performances were assessed by photodegradation of MB, chosen as a model substrate. To demonstrate the catalytic activities of GNCFs, MB degradation was carried out in presence of GNCs, GNCF-100, GNCF-200, and GNCF-300. To 1 mL (4×10^{-6} M) aqueous solution of MB, 4 μL H_2O_2 (50 wt%) was added followed by the addition of 100 μL (1.8 mg mL^{-1}) aqueous suspension of GNCs or GNCFs. A blank sample was also prepared by mixing 100 μL of water instead of catalyst into the mixture of MB (1 mL; 4×10^{-6} M) and H_2O_2 (4 μL ; 50 wt%). The photocatalytic reactions were performed inside a UV chamber, where the samples were irradiated under UV-light, having emission at 350 nm wavelength. A blue LED light (Model no. M455L3-C2) with emission of 455 nm wavelength (power: 360 mW and optical density: 25 mW cm^{-2}) was also used in order to perform the degradation of MB under visible light, where all other conditions remained unaltered. To evaluate photocatalysis performances, UV-visible spectra of each samples were recorded at the interval of 2 min during the reactions. The procedure was repeated with different concentrations of SnCl_2 solutions in water without presence of gold (GNCs or GNCFs). In addition, the catalytic activities were once again performed in the dark environment, where all other conditions remained unaltered.

Supporting Information

Supporting Information is available from the Wiley Online Library or from the author.

Acknowledgements

This work was supported by the Academy of Finland, Centers of Excellence Programme (2014–2019; Grant No. 272361) and Academy Project (Grant No. 310799). S.C. would also like to acknowledge the

provision of facilities and technical support by Aalto University at OtaNano—Nanomicroscopy Center (Aalto NMC).

Conflict of Interest

The authors declare no conflict of interest.

Keywords

bioimaging, bright photoluminescence, gold nanoclusters, metal ions, photocatalysis

Received: April 15, 2019

Revised: June 24, 2019

Published online:

- [1] J. Yao, M. Yang, Y. Duan, *Chem. Rev.* **2014**, *114*, 6130.
- [2] Y. Chan, F. Ye, M. E. Gallina, X. Zhang, Y. Jin, I. Wu, D. T. Chiu, *J. Am. Chem. Soc.* **2012**, *134*, 7309.
- [3] A. Hoshino, K. Fujioka, T. Oku, M. Suga, Y. F. Sasaki, T. Ohta, M. Yasuhara, K. Suzuki, K. Yamamoto, *Nano Lett.* **2004**, *4*, 2163.
- [4] F. Cao, E. Ju, C. Liu, W. Li, Y. Zhang, K. Dong, Z. Liu, J. Ren, X. Qu, *Nanoscale* **2017**, *9*, 4128.
- [5] E. Ju, Z. Liu, Y. Du, Y. Tao, J. Ren, X. Qu, *ACS Nano* **2014**, *8*, 6014.
- [6] F. M. Winnik, D. Maysinger, *Acc. Chem. Res.* **2013**, *46*, 672.
- [7] U. Resch-Genger, M. Grabolle, S. Cavaliere-Jaricot, R. Nitschke, T. Nann, *Nat. Methods* **2008**, *5*, 763.
- [8] I. Chakraborty, T. Pradeep, *Chem. Rev.* **2017**, *117*, 8208.
- [9] R. Jin, C. Zeng, M. Zhou, Y. Chen, *Chem. Rev.* **2016**, *116*, 10346.
- [10] L. Y. Chen, C. W. Wang, Z. Yuan, H. T. Chang, *Anal. Chem.* **2015**, *87*, 216.
- [11] S. Wang, X. Meng, A. Das, T. Li, Y. Song, T. Cao, X. Zhu, M. Zhu, R. Jin, *Angew. Chem., Int. Ed.* **2014**, *53*, 2376.
- [12] K. Pyo, V. D. Thanthirige, K. Kwak, P. Pandurangan, G. Ramakrishna, D. Lee, *J. Am. Chem. Soc.* **2015**, *137*, 8244.
- [13] Z. Luo, X. Yuan, Y. Yu, Q. Zhang, D. T. Leong, J. Y. Lee, J. Xie, *J. Am. Chem. Soc.* **2012**, *134*, 16662.
- [14] N. Goswami, F. Lin, Y. Liu, D. T. Leong, J. Xie, *Chem. Mater.* **2016**, *28*, 4009.
- [15] M. Quintanilla, L. M. Liz-Marzan, *Science* **2018**, *361*, 645.
- [16] J. Lu, C. Aydin, N. D. Browning, B. C. Gates, *Angew. Chem.* **2012**, *124*, 5944.
- [17] X. Kang, S. Wang, Y. Song, S. Jin, G. Sun, H. Yu, M. Zhu, *Angew. Chem., Int. Ed.* **2016**, *55*, 3611.
- [18] Nonappa, T. Lahtinen, J. S. Haataja, T. R. Tero, H. Häkkinen, O. Ikkala, *Angew. Chem., Int. Ed.* **2016**, *55*, 16035.
- [19] A. Chakraborty, A. C. Fernandez, A. Som, B. Mondal, G. Natarajan, G. Paramasivam, T. Lahtinen, H. Häkkinen, Nonappa, T. Pradeep, *Angew. Chem., Int. Ed.* **2018**, *57*, 6522.
- [20] Nonappa, O. Ikkala, *Adv. Funct. Mater.* **2018**, *28*, 1704328.
- [21] Z. Y. Li, N. P. Young, M. D. Vece, S. Palomba, R. E. Palmer, A. L. Bleloch, B. C. Curley, R. L. Johnston, J. Jiang, J. Yuan, *Nature* **2008**, *451*, 46.
- [22] N. B. Shustova, B. D. McCarthy, M. Dinca, *J. Am. Chem. Soc.* **2011**, *133*, 20126.
- [23] N. S. McIntyre, *J. Electron Spectrosc. Relat. Phenom.* **2011**, *184*, 29.
- [24] Y. Yang, A. Han, R. Li, G. Fang, J. Liu, S. Wang, *Analyst* **2017**, *142*, 4486.
- [25] F. Lu, X. Ji, Y. Yang, W. Deng, C. E. Banks, *RSC Adv.* **2013**, *3*, 18791.

- [26] A. Yahia-Ammar, D. Sierra, F. Merola, N. Hildebrandt, X. L. Guevel, *ACS Nano* **2016**, *10*, 2591.
- [27] N. Goswami, Q. Yao, Z. Luo, J. Li, T. Chen, J. Xie, *J. Phys. Chem. Lett.* **2016**, *7*, 962.
- [28] Y. Deng, N. Chen, Q. Li, X. Wu, X. Huang, Z. Lin, Y. Zhao, *Cryst. Growth Des.* **2017**, *17*, 3170.
- [29] H. Lan, Y. Wen, Y. Shi, K. Liu, Y. Mao, T. Yi, *Analyst* **2014**, *139*, 5223.
- [30] M. Nakayama, T. Terahara, M. Wada, K. Harada, A. Sugii, H. Egawa, *J. Appl. Polym. Sci.* **1991**, *43*, 2231.
- [31] H. Cox, A. J. Stace, *J. Am. Chem. Soc.* **2004**, *126*, 3939.
- [32] A. Cantelli, G. Guidetti, J. Manzi, V. Caponetti, M. Montalti, *Eur. J. Inorg. Chem.* **2017**, *2017*, 5068.
- [33] S. Chandra, P. Patra, S. H. Pathan, S. Roy, S. Mitra, A. Layek, R. Bhar, P. Pramanik, A. Goswami, *J. Mater. Chem. B* **2013**, *1*, 2375.
- [34] S. Chandra, G. Beaune, N. Shirahata, F. M. Winnik, *J. Mater. Chem. B* **2017**, *5*, 1363.
- [35] Y. Pan, S. Neuss, A. Leifert, M. Fischler, F. Wen, U. Simon, G. Schmid, W. Brandau, W. Jahnen-Dechent, *Small* **2007**, *3*, 1941.
- [36] A. Woźniak, A. Malankowska, G. Nowaczyk, B. F. Grześkowiak, K. Tuśnio, R. Słomski, A. Zaleska-Medynska, S. Jurga, *J. Mater. Sci.: Mater. Med.* **2017**, *28*, 92.
- [37] L. Shang, K. Nienhaus, G. U. Nienhaus, *J. Nanobiotechnol.* **2014**, *12*, 5.
- [38] E. E. Connor, J. Mwamuka, A. Gole, C. J. Murphy, M. D. Wyatt, *Small* **2005**, *1*, 325.
- [39] T. Mironava, M. Hadjiargyrou, M. Simon, V. Jurukovski, M. H. Rafailovich, *Nanotoxicology* **2010**, *4*, 120.
- [40] R. Ullah, J. Dutta, *J. Hazard. Mater.* **2008**, *156*, 194.
- [41] J. Zhang, L. Qu, G. Shi, J. Liu, J. Chen, L. Dai, *Angew. Chem., Int. Ed.* **2016**, *55*, 2230.
- [42] W. Kurashige, R. Kumazawa, D. Ishii, R. Hayashi, Y. Niihori, S. Hossain, L. V. Nair, T. Takayama, A. Iwase, S. Yamazoe, T. Tsukuda, A. Kudo, Y. Negishi, *J. Phys. Chem. C* **2018**, *122*, 13669.
- [43] Nonappa, J. S. Haataja, J. V. I. Timonen, S. Malola, P. Engelhardt, N. Houbenov, M. Lahtinen, H. Häkkinen, O. Ikkala, *Angew. Chem., Int. Ed.* **2017**, *56*, 6473.
- [44] D. Mastronarde, *Microsc. Microanal.* **2003**, *9*, 1182.
- [45] J. R. Kremer, D. N. Mastronarde, J. R. McIntosh, *J. Struct. Biol.* **1996**, *116*, 71.
- [46] P. Engelhardt, in: *Electron Microscopy: Methods and Protocols*, 2nd edition, (Ed: J. Kuo), Methods in Molecular Biology, Vol. 369, Humana Press Inc., Totowa, NJ **2007**, pp. 365–385.